CHAPTER 5 EXPERIMEATAL RESULTS AND DISCUSSION

The objective of this chapter is to present the results and discussion of the heat transfer characteristics of R134a inside microchannel heat sink. The results of the present study were divided into main three parts.

5.1 Single phase heat transfer validation tests

The experimental apparatus was specially constructed for this study. Therefore, the energy balance obtained across the test section assembly was first evaluated for single-phase fluid flow, in order to establish confidence in the experimentally-determined heat transfer coefficients. A series of single-phase experiments were conducted with different mass fluxes and heat transfer rates supplied to the test section. Fig. 4 shows the amount of absorbed heat. As seen from the figure, the differences between the heat applied to the microchannel's heat sink $\left(Q_{\text{elec}}\right)$ and the heat absorbed by the refrigerant $\left(Q_{\text{ref}} = \dot{m} c_{\text{p}} \left(T_{\text{ref,out}} - T_{\text{ref,in}}\right)\right)$ did not exceed 5%, in most cases. This result indicates that the heat losses to the surroundings were negligible, although the mass flow rates of the working fluid varied.

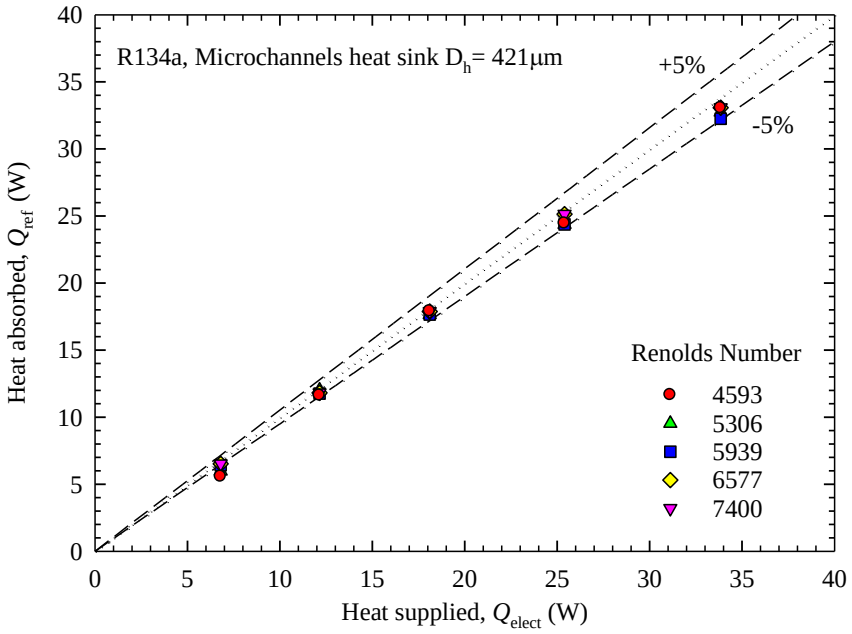

Figure 5.1 Energy balance between electrical heat supplied and heat absorbed during a single phase tested

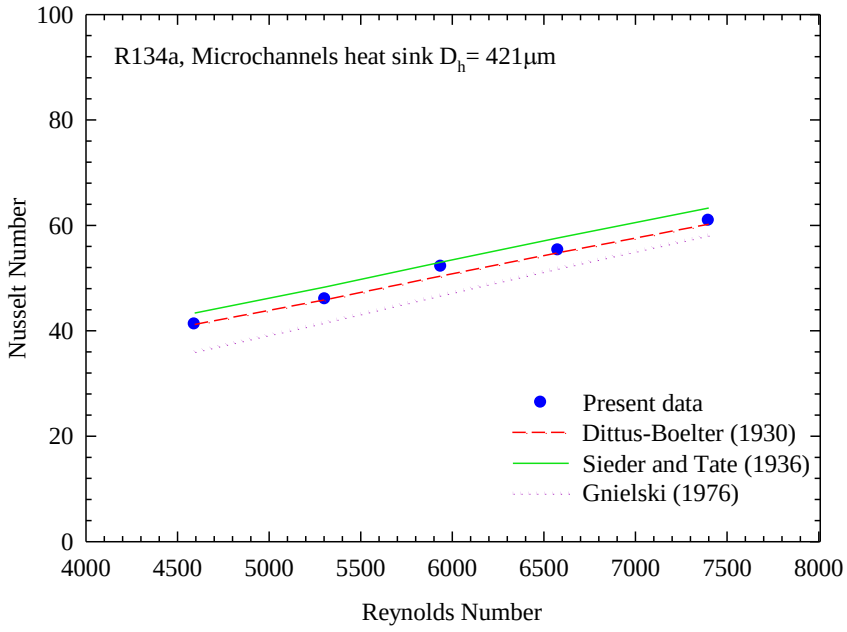

Figure 5.2 Comparison between the data obtained by the experimental set up and single phase heat transfer correlations from the literature

Moreover, to investigate the accuracy of the experimental setup, the variance of the Nusselt number with the Reynolds number was examined for a single-phase flow of R-134a. Fig.5 presents the comparison between the data obtained by the experimental setup with the prediction from the well-known and commonly used correlations from Dittus-Boelter (1930), Sieder and Tate (1936) and Gnielski (1976)as presented in Incropera and DeWitt (2007). A good agreement was observed between the present data and the results of former works.

5.2 Heat transfer characteristic of R134a during flow boiling in micro-channel

5.2.1 Boiling curves

In order to investigate the dominant heat transfer mechanism during flow boiling, boiling curves were constructed from the measurements in the test piece. The variation in wall heat flux with the temperature differences between the wall and the saturation temperature are illustrated in Fig.5.3 and Fig.5.4. The results were obtained for three different mass fluxes ranging from 400-1200 kg/m^2s, heat fluxes from 14.3-168.4 kW/m^2, and saturation temperatures of 18 ^oC and 23 ^oC. The inlet quality was held constant at approximately 0.1 throughout the experiment.

As indicated in the Fig.5.3 and Fig.5.4, the curves for mass fluxes of 800 and 1200 kg/m^2 s merge into a single curve, irrespective of the saturation temperature. This indicates the dominance of nucleate boiling over convective heat transfer. Generally, in a nucleate boiling regime, isolated bubbles are formed by nucleation in the superheated liquid near the walls before departing from the surface. The heat transfer coefficient in

this mode of boiling is a function of heat flux, but is almost independent of mass flux or vapor quality.

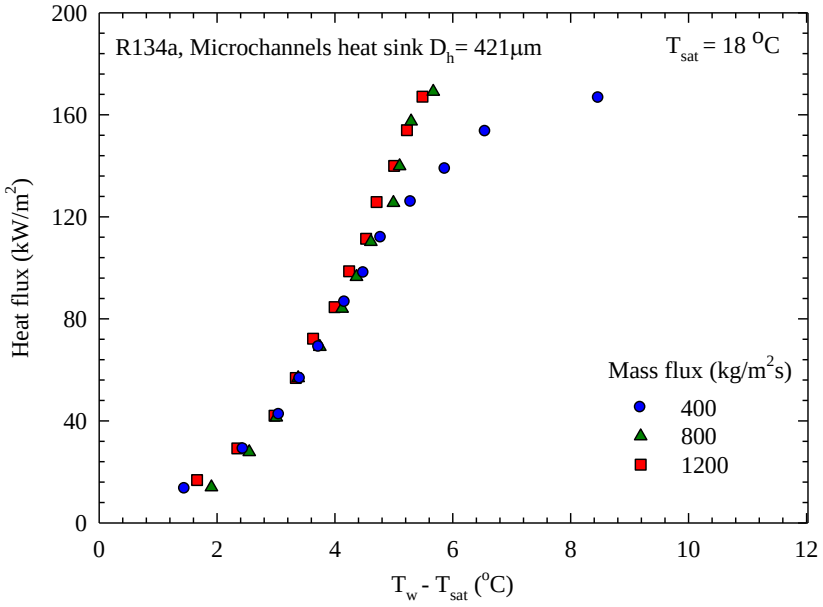

Figure 5.3 Boiling curves at saturation temperature of 18 °C for difference three mass fluxes from 400-1200 kg/m^2 s.

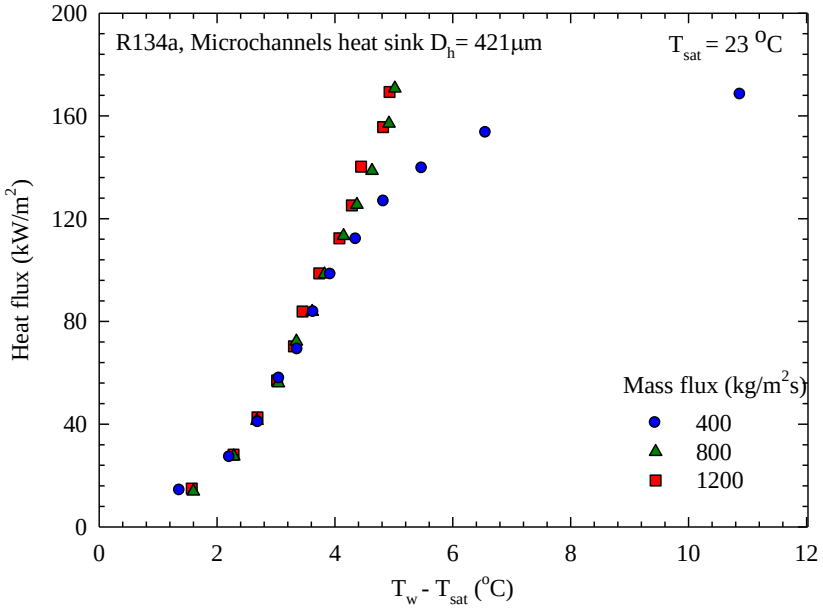

Figure 5.4 Boiling curves at saturation temperature of 23 °C for difference three mass fluxes from 400-1200 kg/m^{2}s.

By contrast, the mass flux of 400 kg/m^{2}s was different from the heat flux trend when the excess temperature was higher than about 4 ^{o}C. At this point, the curve was found to deviate from the boiling regime. This indicates that convective boiling had a certain influence on boiling mechanism. These trends are quite similar to those found by Chen and Garimella (2006).

5.2.2 Effects of relevant parameters on average heat transfer coefficient

In order to investigate the overall performance of the heat exchanger, average heat transfer coefficients are required. So, the heat transfer coefficients of R134a in an extruded microchannel are examined as an average value over the entire length. The effect of relevant parameters, including mass flux, heat flux, saturation temperature, and inlet vapor quality, on the average heat transfer coefficient of R134a during flow boiling in a microchannel heat sink are examined and discussed. Experimental results were obtained for three difference mass fluxes of 400, 800 and 1200 kg/m^2 s, wall heat fluxes from 14.3–168.4 kW/m^2, saturation temperatures of 13, 18, and 23 ^{o}C, and inlet vapor quality between 0.05 and 0.93.

Figure 5.5 and 5.6 illustrate the effect of mass flux on average heat transfer coefficient as a function of wall heat flux for the different saturation temperatures of 18 ^{o}C (Fig.5.5) and 23 ^{o}C (Fig.5.6), and mass fluxes in the range of 400–1200 kg/m^{2}s, while the inlet vapor quality was held at a constant 0.1 throughout the experiment. For the mass fluxes of 800 and 1200 kg/m^{2}s, the heat transfer coefficient was independent of mass fluxes. On the contrary, the heat transfer coefficient increased when increasing heat flux over the range of heat fluxes tested. However, for the mass flux of 400 kg/m^2 s, the decrease in the heat transfer coefficient was detected when the heat flux was increased to more

than about 110 kW/m^2, which was due to an early, partial dry out of the side wall. As annotated in the Fig.5.5 and Fig.5.6, these results show a drop in the heat transfer coefficient.

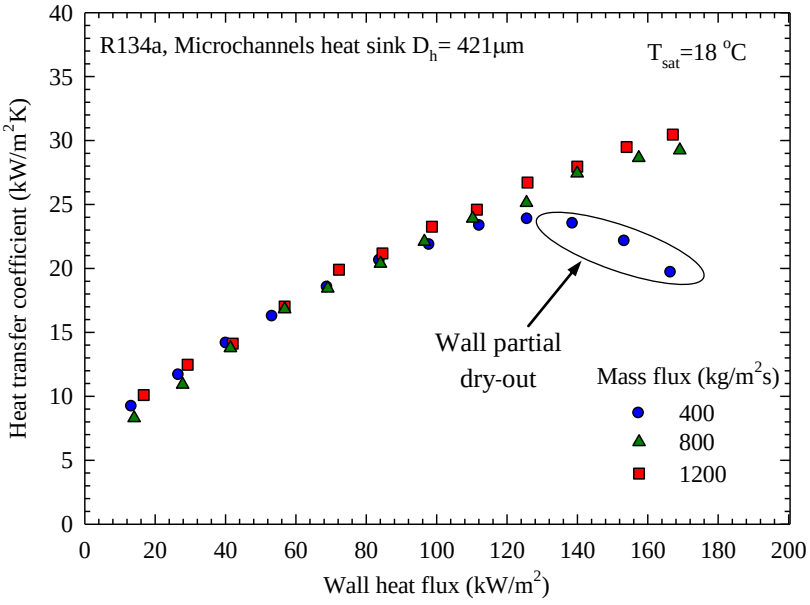

Figure 5.5 The effect of heat flux and mass flux on heat transfer coefficient having a saturation temperature of 18 °C

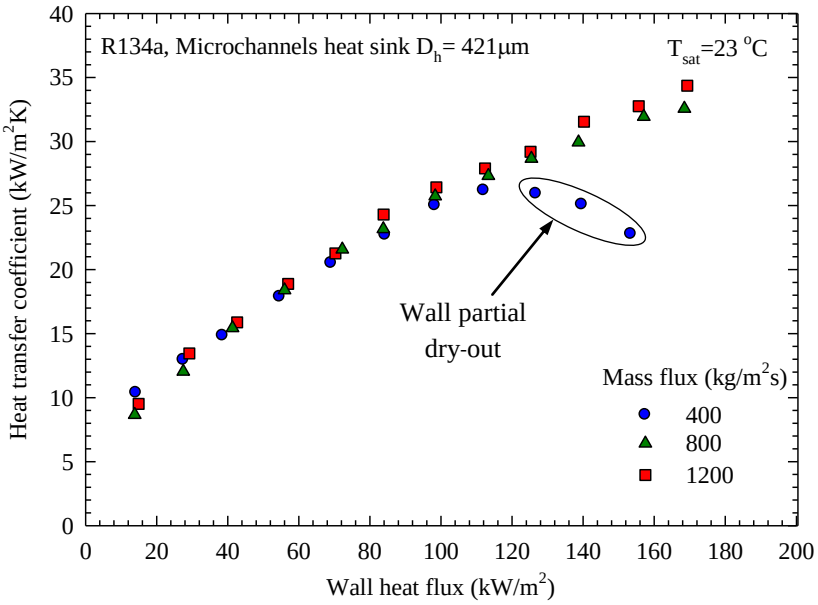

Figure 5.6 The effect of heat flux and mass flux on heat transfer coefficient having a saturation temperature of 23 ^{o}C

In the results as shown in Fig. 5.5-5.6, similar observations were also reported by Harirchain and Garimella (2008). In their report, this behavior was attributed to the dominance of the nucleate boiling regime after the onset of boiling, as well as the dominance of convective boiling at the location where each curve begins to deviate from the others. The above conclusions support the experimental results of this study that nucleate boiling is an important boiling mechanism with a certain influence on heat transfer in the boiling process.

The effect of saturation temperature on the average heat transfer coefficient is illustrated for the different mass fluxes between 800 and 1200 kg/m^2 s, corresponding to Fig. 5.7 and Fig. 5.8, respectively. Three different saturation temperatures of 13 ^{o}C, 18 ^{o}C, and 23 ^{o}C were tested. An inspection of the experimental results in Fig. 5.7 and Fig. 5.8 indicates that the heat transfer coefficient increased when heat flux increased. The

saturation temperature had a significant effect on the heat transfer coefficient. For heat fluxes more than 60 kW/m^2, the heat transfer coefficients of 18 ^{o}C and 23 ^{o}C were higher than those of 13 ^{o}C by about 7–15% and 18–25%, respectively.

These results are similar to those already observed in the literature for R134a flow boiling in minichannels by Choi et al. (2007), Shiferaw et al. (2009), Tibiriçá (2010). From the study of Sharma et al. (1996), this increase could be attributed to the increase of saturation temperature, which led to the decrease of bubble departure diameter caused by boiling. Moreover, the increase of saturation temperature also increased the bubble departure frequency. In addition, the bubbles could depart from the channel wall more quickly at higher saturation temperatures. Additionally, in general nucleate boiling, the flow turbulence caused departure from the wall, which also led to better heat transfer.

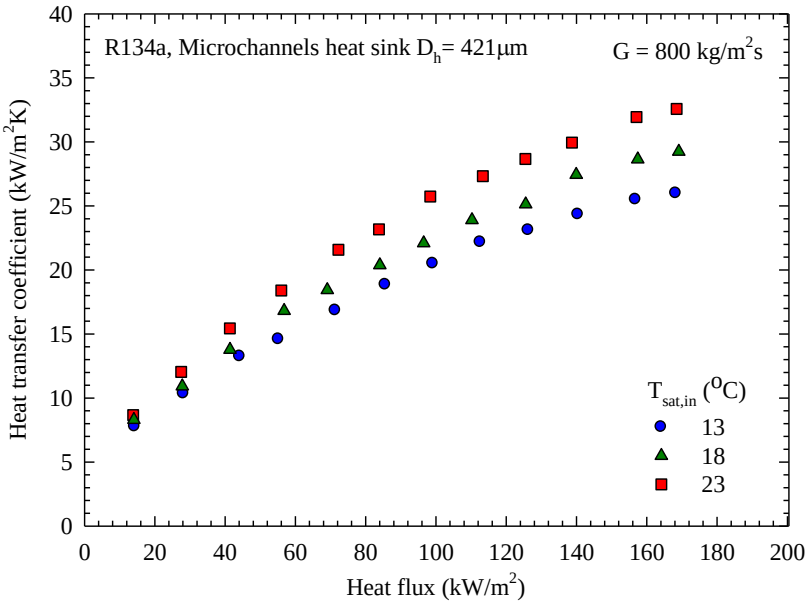

Figure 5.7 Effect of saturation temperature on average heat transfer coefficient having a mass flux of 800 kg/m^2 s

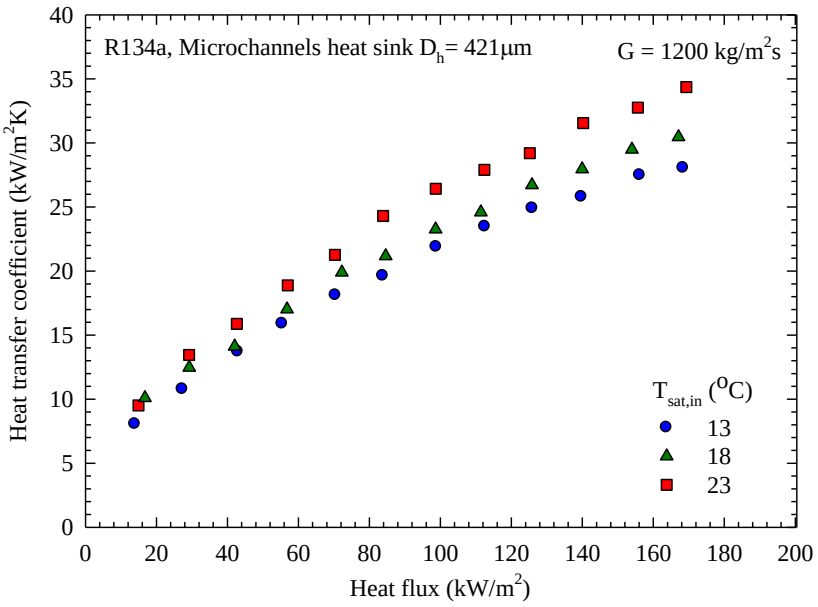

Figure 5.8 Effect of saturation temperature on average heat transfer coefficient having a mass flux of 1200 kg/m^2 s

Figure 5.9-5.10 displays the effect of inlet vapor quality on the heat transfer coefficient for R134a. The results were obtained for a fixed saturation temperature of 23 ^{o}C, mass fluxes ranging from 400–1200 kg/m^2 s, and heat fluxes of 27.1 kW/m^2 (Fig.5.9) and 73.2 kW/m^2 (Fig.5.10). During the experiment, the mass flux, saturation temperature, and heat flux were held constant, while the inlet vapor quality was varied.

The result reveals that, in low/moderate quality regions, the heat transfer coefficient is independent of mass flux. After the moderate quality regions, the heat transfer coefficients start to increase as mass flux and vapor quality increase. These trends are similar to those found by Kuo-Wang (1996), Bao et al. (2000), and Choi et al. (2007). In addition, our result also shows that the distribution of the heat transfer coefficient for a heat flux of 27.1 kW/m^2 is slightly different from that for a heat flux of 73.2 kW/m^2, at an inlet vapor quality higher than about 0.3. Moreover, the effect of mass flux on the

heat transfer coefficient appears at moderate/high inlet vapor quality, wherein the effect is high as vapor quality increases. A higher mass flux results in a greater heat transfer coefficient at moderate/high inlet vapor quality, due to the increase in convective boiling contribution.

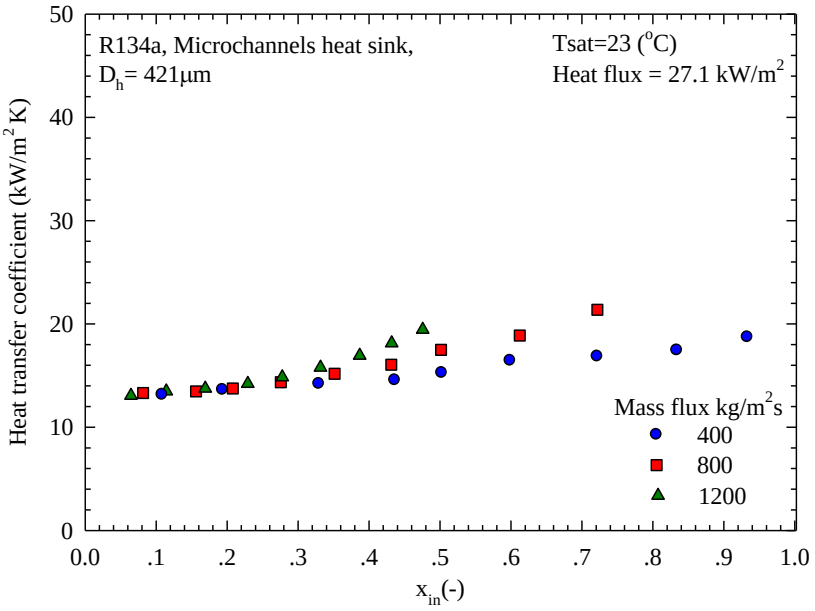

Figure 5.9 Effect of varying inlet quality on average heat transfer coefficient for fixed heat flux of 27.1 kW/m^2

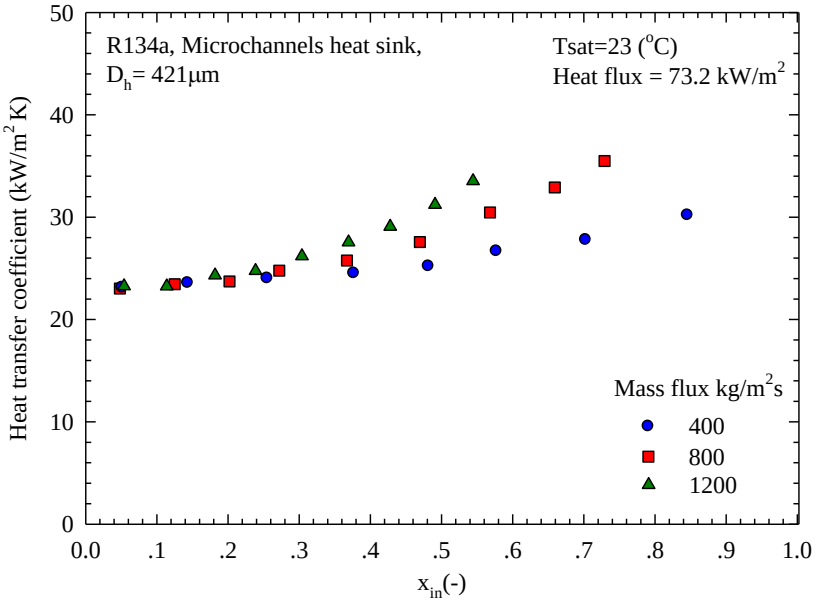

Figure 5.10 Effect of varying inlet quality on average heat transfer coefficient for fixed heat flux of 73.2 kW/m^2

5.2.3 Comparison of experimental heat transfer data with existing correlations

In this section, the experimental results of this work are compared to the results predicted by the existing correlations from the literature for the same operational conditions. The predictive accuracy of the correlation was evaluated by the mean absolute error (MAE), defined as

$$\mathrm{MAE} = \frac{1}{N}\sum \frac{\left|h_{\mathrm{tp,pre}} - h_{\mathrm{tp,exp}}\right|}{h_{\mathrm{tp,exp}}} \times 100\% \qquad (5.1)$$

In addition, the amount of predicted heat transfer coefficients that fall within ±30% of the measured data was determined and defined as ψ. The saturated flow boiling heat transfer correlations of Kandlikar and Balasubramanian (2004), Kim and Mudawar

(2013) and Fang (2013)were considered. All three correlations developed for minichannels and microchannel are summarized in Table 5.1, including the working fluid, the description of the tested geometries, and the evaluation results.

Table 5.1 Correlations for flow boiling heat transfer coefficient.

Author(s)	Working fluids	D_h (mm)	MAE (%)	ψ (%)
Lazarek and Black (1982)	R113	3.1	24.25	73.8
Kandlikar and Balasubramanian (2004)	R113, R134a, R123, R141b, Water	0.19-2.92	12.03	95.1
Kim and Mudawar (2013)	FC72, R11, R113, R123, R1234yf, R1234ze, R134a, R152a, R22, R236fa, R245fa, R32, R404A, R470C, R410A, R147A, CO_2, water	0.19-6.5	22.44	90.3
Fang (2013)	R134a	0.19-8	10.41	100

As shown in Fig. 5.11 to Fig.5.13, the comparison of experimental results with all 3 correlations showed that nearly all of the data deviated by ±30%. The correlation found by Fang (2013) provided the best prediction because it had the lowest MAE value (10.41%) and the largest amount of data falling within 30% of the error band (100%). Fang (2013) had developed a correlation based on a database of 19 published papers mentioned in the R134a flow boiling section. However, the correlations of Kandlikar and Balasubramanian (2004) and Kim and Mudawar (2013) could not predict as well as

the correlation of Fang (2013). Yet, overall, all 3 correlations could predict the presented experimental results well and showed the reliability of the experimental results presented in this study.

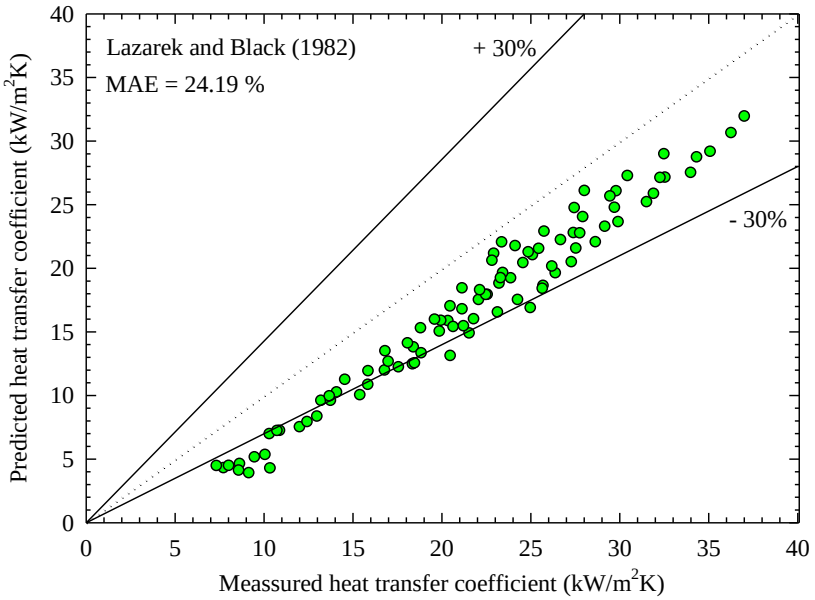

Figure 5.11 The comparison of the experimental data with predicted heat transfer coefficient using Lazarek and Black (1982)

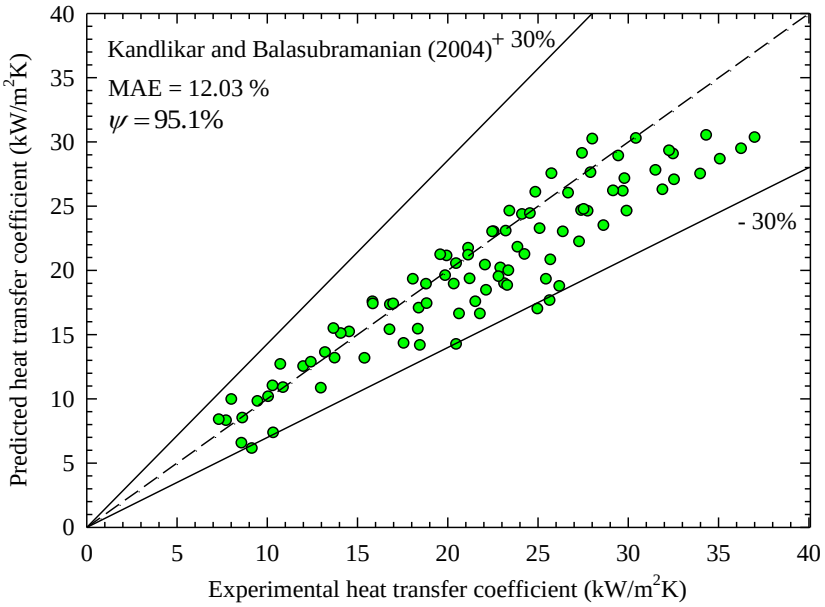

Figure 5.12 The comparison of the experimental data with predicted heat transfer coefficient using Kandlikar and Balasubramanian (2004)

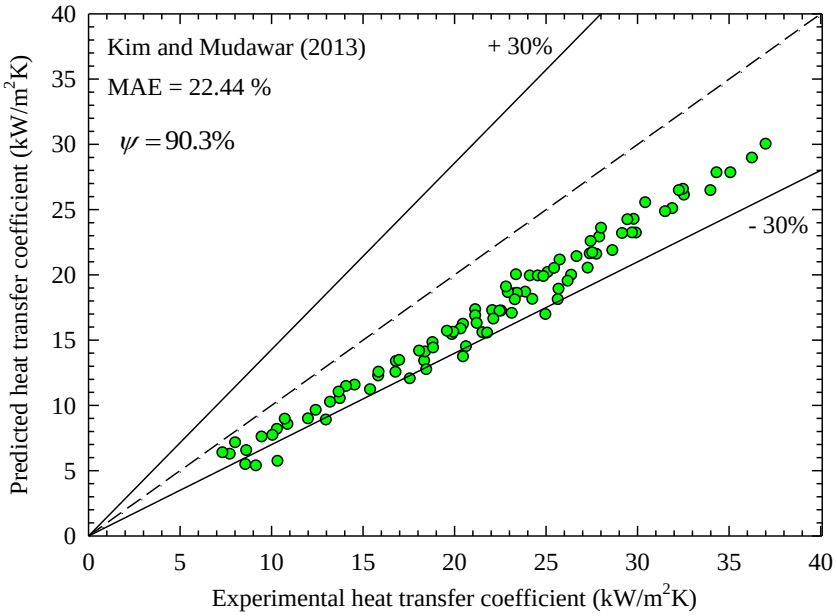

Figure 5.13 The comparison of the experimental data with predicted heat transfer coefficient using Kim and Mudawar (2013)

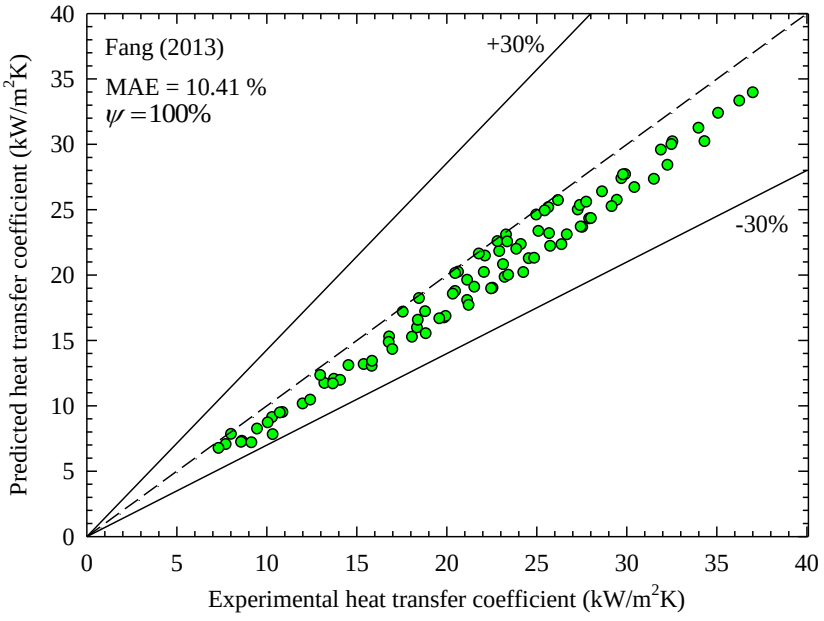

Figure 5.14 The comparison of the experimental data with predicted heat transfer coefficient using Fang (2013)

5.2.4 Proposed heat transfer coefficient correlation

In this section, a new correlation is developed from all experimental data to improve the accuracy of predicting the average heat transfer coefficient of R134a during boiling in a multiport microchannel heat sink. The correlation is expressed as follow:

$$h = \frac{11162 Bo^{0.509} We_l^{0.291}}{\left(\rho_l / \rho_v\right)^{0.465}} \frac{k_l}{D_h} \tag{5.2}$$

Where Bo and We_{lo} are the Boiling number and Webber number, respectively, defined as follow:

$$Bo = \frac{q''}{h_{fv} G} \tag{5.3}$$

And

$$We_{lo} = \frac{G^2 D_h}{\rho_l \sigma} \tag{5.4}$$

The comparison of the proposed heat transfer coefficient correlation with present measure data is shown in Fig.5.15. It is clear from this figure that more than 95% of the data measured from the present study falls within ±10% of the proposed correlation.

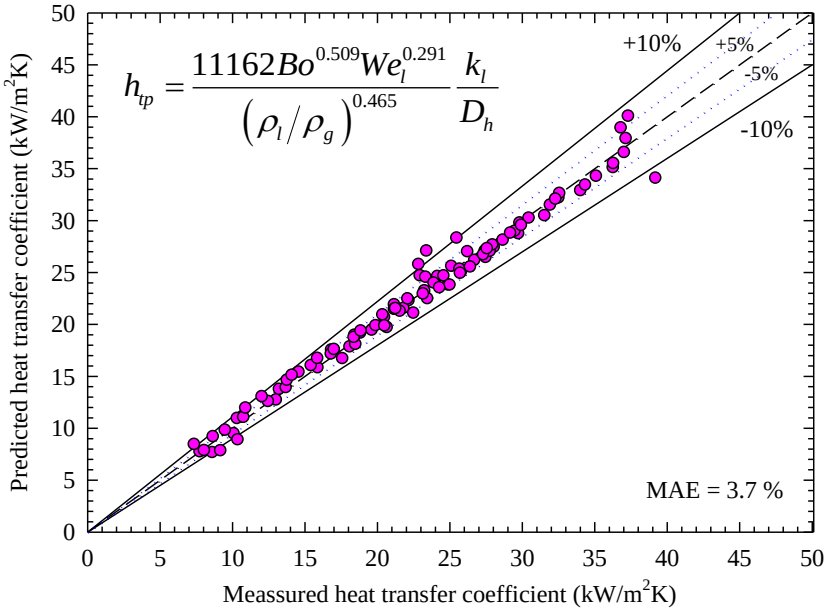

Figure 5.15 Predicted heat transfer coefficient using the proposed correlation versus the experimental data.

5.3 Pressure drop characteristics of R134a during flow boiling in microchannel

In this section, the characteristics of the pressure drop in microchannel are presented. The pressure drop for the microchannel is measured and compared to the available correlations. The measured pressure drop is corrected for the entrance and exit losses and only the pressure drop for the microchannel alone is presented. The Darcy Friction Factor is used for the predicted result. In addition, a property correction factor has been applied to investigate if it is valid for microchannel.

5.3.1 Pressure drop components

The total pressure drop across the test section are composed of the four main components, i.e., the frictional pressure drop, the accelerational pressure drop, the sudden contraction pressure drop and the sudden expansion pressure drop. The

components of the total pressure drop along the microchannel test section with the variation of heat fluxes are presented in Fig. 5.15 and Fig. 5.16. The results were obtained at the mass flux of 800 and 1200 kg/m^{2}s and the saturation temperature was kept constant at 18 ^{o}C. For a constant mass flux, the results show that the frictional pressure drop is dominant over the other three components for all conditions. In addition, these figures also show the same trend that the frictional pressure drop increase with increasing the supposed heat flux. The possible reason for this phenomenon is that as heat flux increase the number of bubbles at channel wall surface also increases which is attributed to the increasing of vapor velocity and results in the increasing of frictional pressure drop.

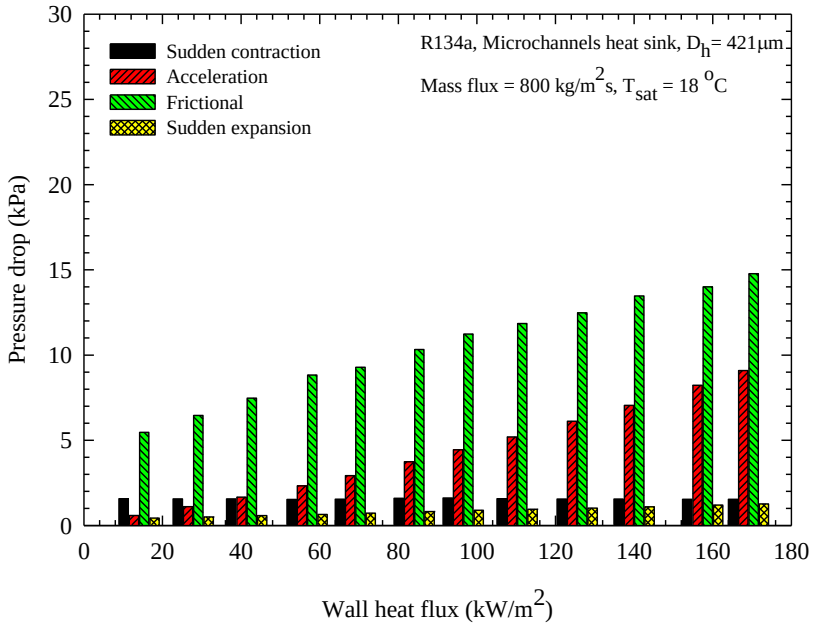

Figure 5.16 Individual components of pressure drop as a function heat flux at the mass flux of 800 kg/m^2 s

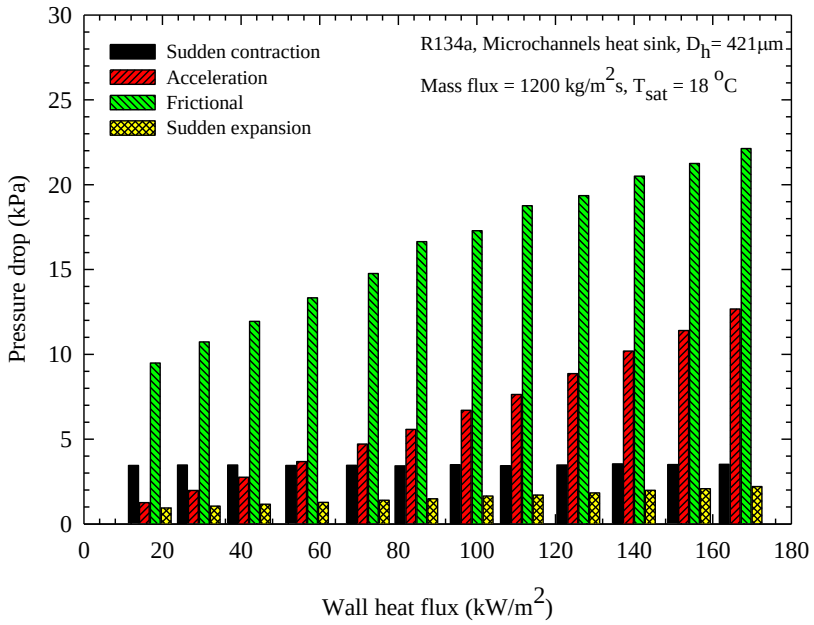

Figure 5.17 Individual components of pressure drop as a function heat flux at the mass flux of 1200 kg/m^2 s

5.3.2 Effects of relevant parameters on frictional pressure gradient

Variations of frictional pressure gradient with heat flux are presented in the Fig.5.17 and Fig.5.18 for a different saturation temperature of 13 ^{o}C and 23 ^{o}C, respectively. The results indicate that the frictional pressure gradient increase with an increasing heat flux. The increasing heat flux results in a higher vaporization and then leads to an increase in the fluid vapor quality and flow velocity. Moreover, for a constant heat flux, these figures also revealed that the pressure gradient increases when the mass flux increases. This is due to higher shear stress at the channel wall and interfacial shear at the liquid-vapor interface.

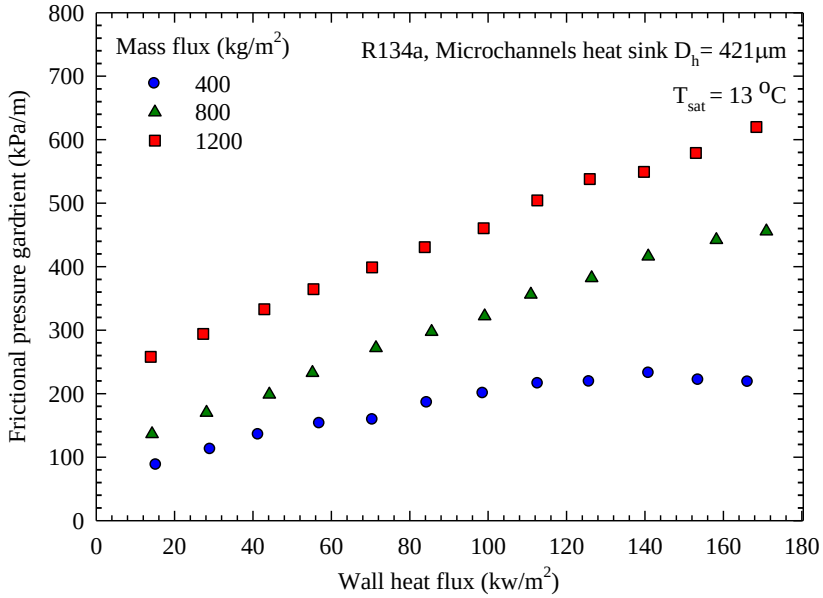

Figure 5.18 The effect of wall heat flux and mass flux on frictional pressure drop having a saturation temperature of 13 ^{o}C

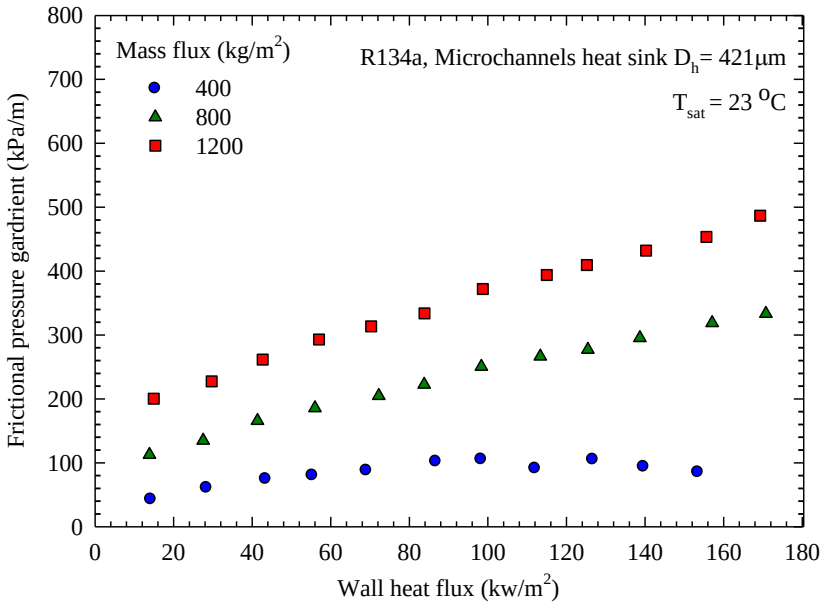

Figure 5.19 The effect of wall heat flux and mass flux on frictional pressure drop having a saturation temperature of 23 ^{o}C

Figure 5.19 and 5.20 illustrate the influence of saturation temperature on the frictional pressure gradient. At constant mass flux and heat flux, the results indicate that the

frictional pressure gradient increases with decreasing saturation temperature. This can be explained by the difference in the properties of the liquid and vapor phase. As the saturation temperature is decreased from 23 to 13 ^{o}C, it found that the viscosity ratio, μ_l/μ_v , increases from 17.3 to 20.4 (17.8%), and the density ratio, ρ_l/ρ_v , increases from 39.8 to 56.1 (40.7%). The increases of liquid density and liquid viscosity result in a lower liquid velocity, whereas the decreasing vapor density and vapor viscosity result in higher vapor velocity. Moreover, surface tension forces are more dominant at lower temperature; thus, the interface between liquid and vapor is less wavy. At lower temperature, the pressure drop increases because of higher liquid viscosity and an increase relative phase densities. The result is a higher interfacial shear. Therefore, the frictional pressure gradients increase when saturation temperature decreases.

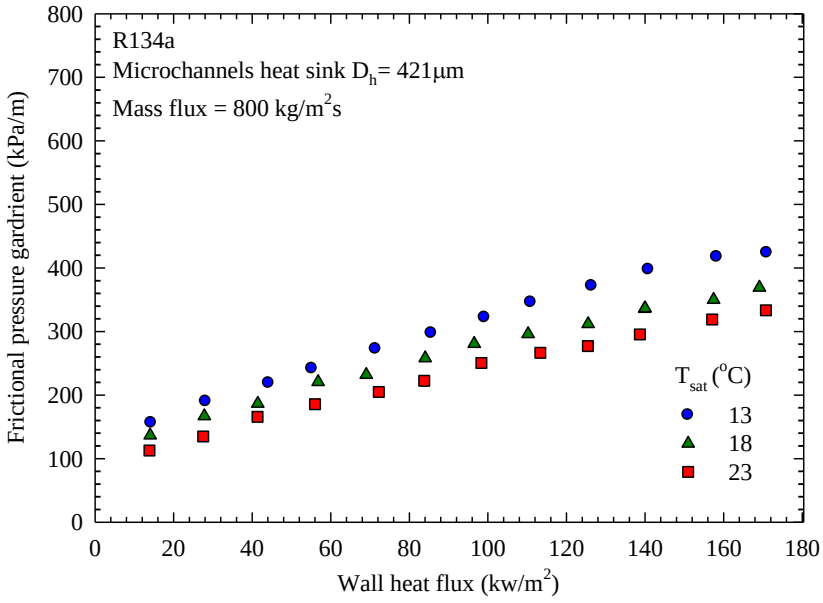

Figure 5.20 The effect of wall heat flux and saturation temperature on frictional pressure drop having a mass flux of 800 kg/m^2 s

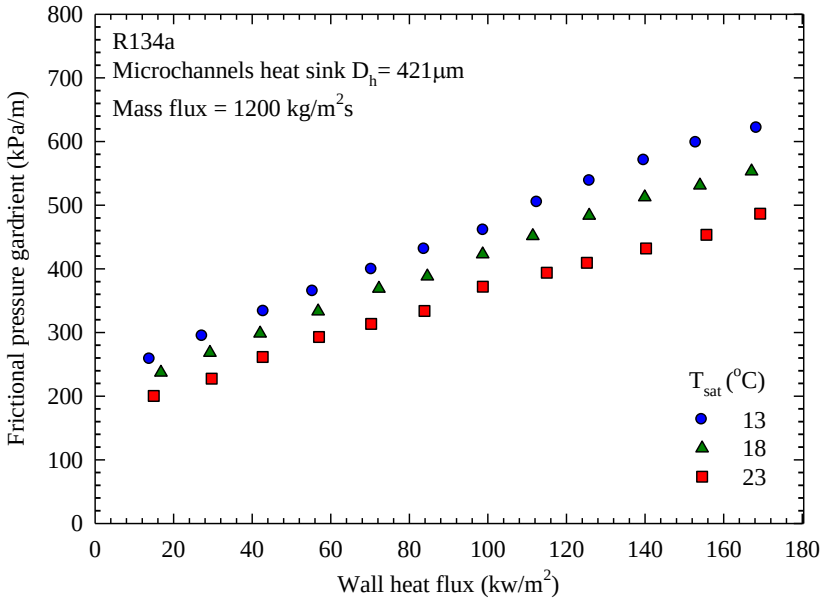

Figure 5.21 The effect of wall heat flux and saturation temperature on frictional pressure drop having a mass flux of 1200 kg/m^2 s

Figure 5.21 shows the frictional pressure gradient of R134a as a function of inlet vapor quality at a saturation temperature of 23 ^{o}C, a heat flux of 27.1 kW/m^2 and mass flux between 400 and 1200 kg/m^{2}s. Figure 5.21 reveals that, for the mass flux of 400 kg/m^{2}s, the frictional pressure drop increases slightly with inlet vapor quality. For the higher mass flux, an increase of frictional pressure drop is observed when the inlet vapor quality is increased. This is because, at higher vapor quality, the higher velocity of the vapor flow causes more shear stress at the interface of the vapor and liquid film. Moreover, the increase of mass flux will also increase the vapor velocity and flow turbulence. For this reason the pressure drop is increased.

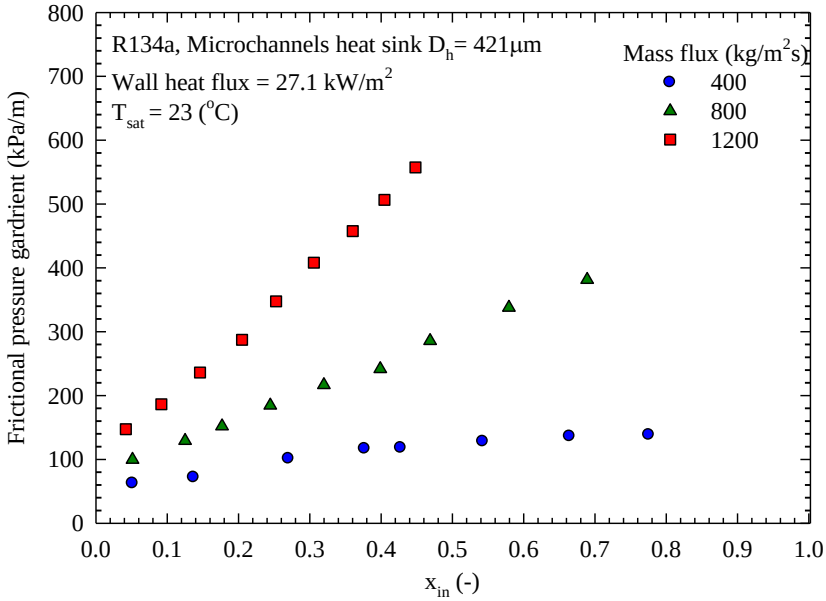

Figure 5.22 The effect of inlet vapor quality on frictional pressure drop for a heat flux of 27.1 kW/m^2 and saturation temperature of 23 ^{o}C

5.3.4 Comparison of experimental frictional pressure drop data with existing correlations

The frictional pressure drop data obtained from the present study are compared with the values predicted by both homogeneous flow and separated flow models. In this study, however, the pressure drop predictions based on the separated flow model are found to be less predictable for the present data when compared with those from the homogeneous flow model.

For homogeneous flow assumption which was found to be in good agreement with the experimental data, the homogeneous flow model assumes that vapor and liquid phases flow with equal velocity. The vapor-liquid mixture is considered as a single phase flowing with average fluid properties. For the pressure drop calculations based on homogeneous flow, it follows that

$$-\left(\frac{dP}{dz}\right)_{\mathrm{F}} = \frac{G^2 f_{\mathrm{tp}}}{2D_{\mathrm{h}}\rho_{\mathrm{h}}} \tag{5.5}$$

$$\rho_{\mathrm{h}} = \left(\frac{x}{\rho_{\mathrm{v}}} + \frac{(1-x)}{\rho_{\mathrm{l}}}\right)^{-1} \tag{5.6}$$

In Eqs.(5.2) and (5.3), $-(dP/dz)_{\mathrm{F}}$ is the two-phase frictional pressure gradient, G is mass flux, D_{h} is the hydraulic diameter, x is vapor quality, ρ_{h} is the average density of the homogenous fluid, and ρ_{l} and ρ_{v} are the liquid and vapor density, respectively. In Eq.(5.2), f_{tp} represents the two-phase Darcy friction factor which is a function of the two-phase Reynolds number:

$$\mathrm{Re}_{\mathrm{tp}} = \frac{GD_{\mathrm{h}}}{\mu_{\mathrm{tp}}} \tag{5.7}$$

For laminar flow ($\mathrm{Re}_{\mathrm{tp}} < 2000$),

$$f_{\mathrm{tp}} = 64\,\mathrm{Re}_{\mathrm{tp}}^{-1} \tag{5.8}$$

For turbulent flow ($\mathrm{Re}_{\mathrm{tp}} \geq 2000$) in a smooth channel,

$$f_{\mathrm{tp}} = 0.3164\,\mathrm{Re}_{\mathrm{tp}}^{-0.25} \tag{5.9}$$

where μ_{tp} presented in Eq.(5.4) is the two-phase mixture viscosity. Several two-phase mixture viscosity models proposed by different researcher are summarized in Table 5.1. Moreover, the assessment of all correlations based on the homogeneous model used for comparison in this study is shown in the Table 5.2.

Table 5.2 Two-phase viscosity correlations employed in the homogeneous model

Author(s)	Two-phase mixture viscosity correlations
McAdams et al. (1942)	$\mu_{tp} = \left(\frac{x}{\mu_v} + \frac{1-x}{\mu_l} \right)^{-1}$
Cicchitti et al. (1960)	$\mu_{tp} = x\mu_v + (1-x)\mu_l$
Owens (1961)	$\mu_{tp} = \mu_l$
Dukler et al. (1964)	$\mu_{tp} = \omega\mu_v + (1-\omega)\mu_l,\ \omega = \frac{x\upsilon_v}{\upsilon_l + x\upsilon_{lv}}$
Beattie and Whalley (1982)	$\mu_{tp} = \omega\mu_v + (1-\omega)(1+2.5\omega)\mu_l$
Lin et al. (1991)	$\mu_{tp} = \frac{\mu_l\mu_v}{\mu_v + x^{1.4}(\mu_l - \mu_v)}$
Awad and Myuztchka (2008)	$\mu_{tp} = \mu_v \frac{2\mu_v + \mu_l - 2(\mu_v - \mu_l)(1-x)}{2\mu_v + \mu_l + (\mu_v - \mu_l)(1-x)}$

Table 5.3 Assessment of the homogeneous model with different viscosity model

Viscosity model's	MAE (%)	Percentage of data within ±30% range
McAdams et al. (1942)	18.8	84.5
Cicchitti et al. (1960)	27.8	67.0
Owens (1961)	39.6	41.7
Dukler et al. (1964)	22.9	74.8
Beattie and Whalley (1982)	18.7	84.5
Lin et al. (1991)	19.3	79.6
Awad and Myuztchka (2008)	19.4	79.6

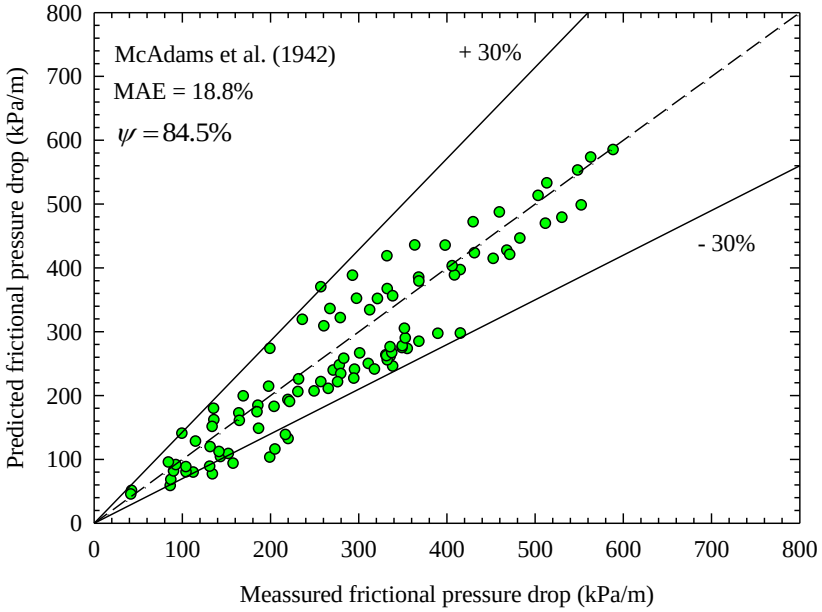

Figure 5.23 The comparison of the experimental data with existing correlation proposed by McAdams et al. (1942)

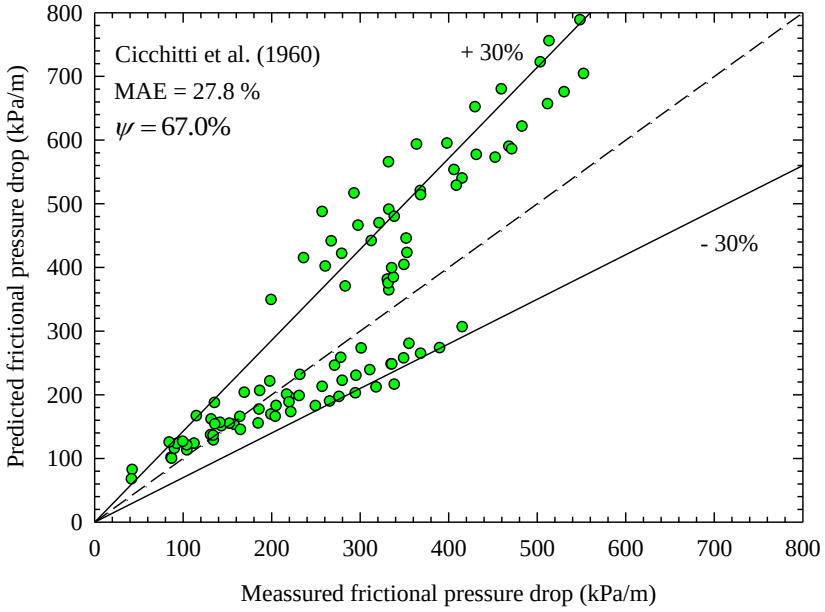

Figure 5.24 The comparison of the experimental data with existing correlation proposed by Cicchitti et al. (1960)

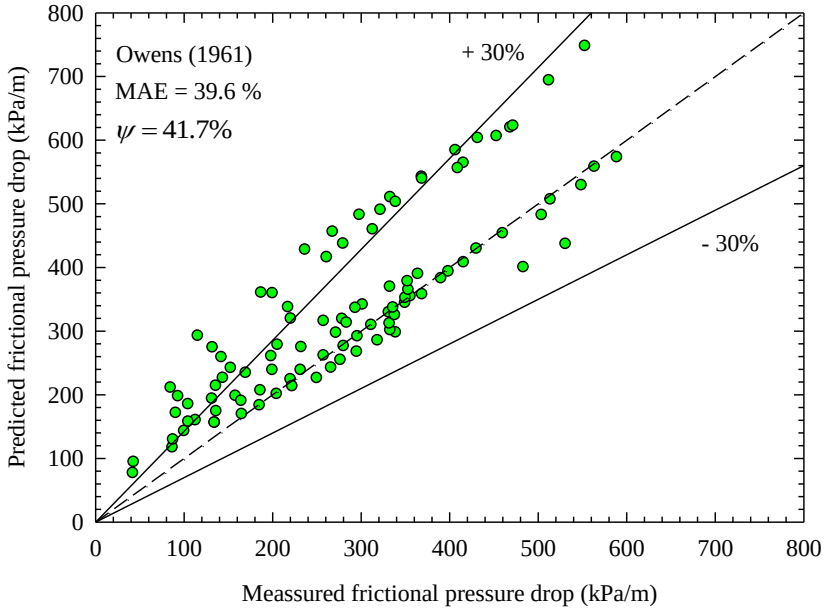

Figure 5.25 The comparison of the experimental data with existing correlation proposed by Owens (1961)

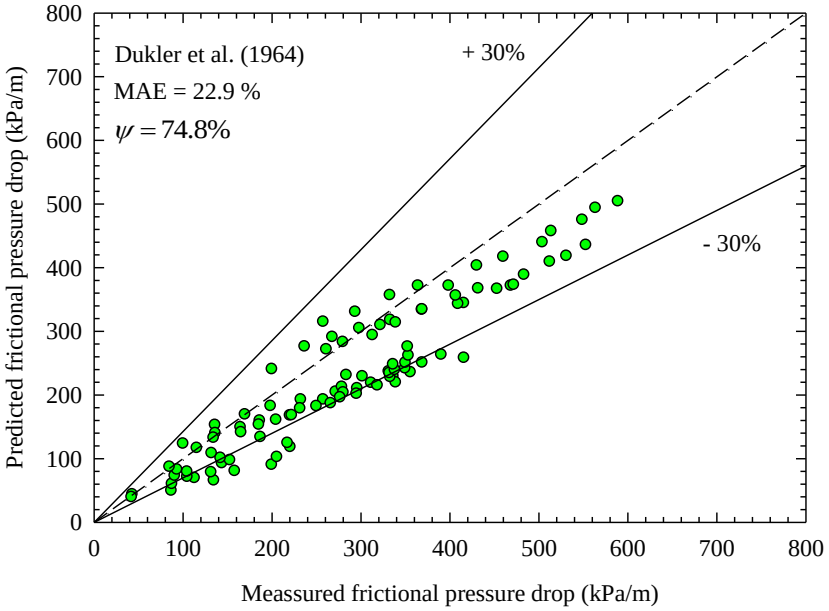

Figure 5.26 The comparison of the experimental data with existing correlation proposed by Dukler et al. (1964)

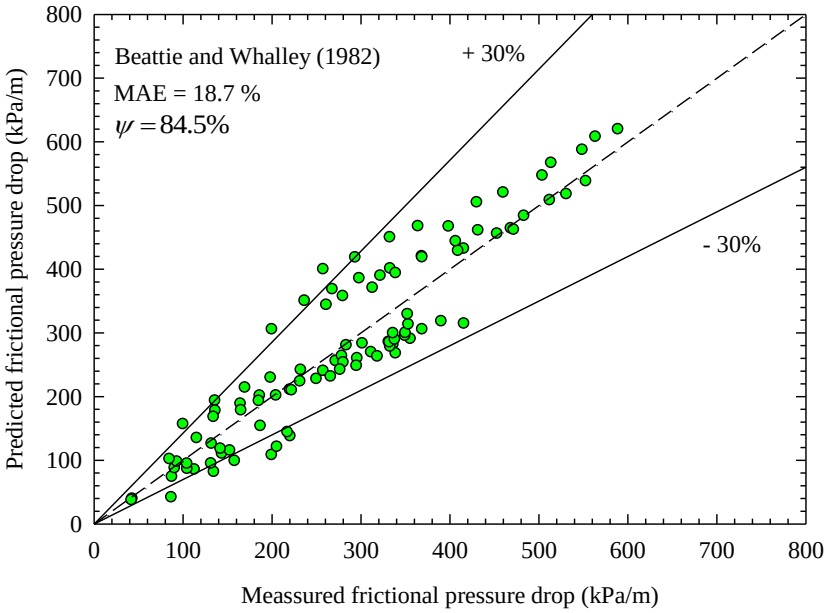

Figure 5.27 The comparison of the experimental data with existing correlation proposed by Beattie and Whalley (1982)

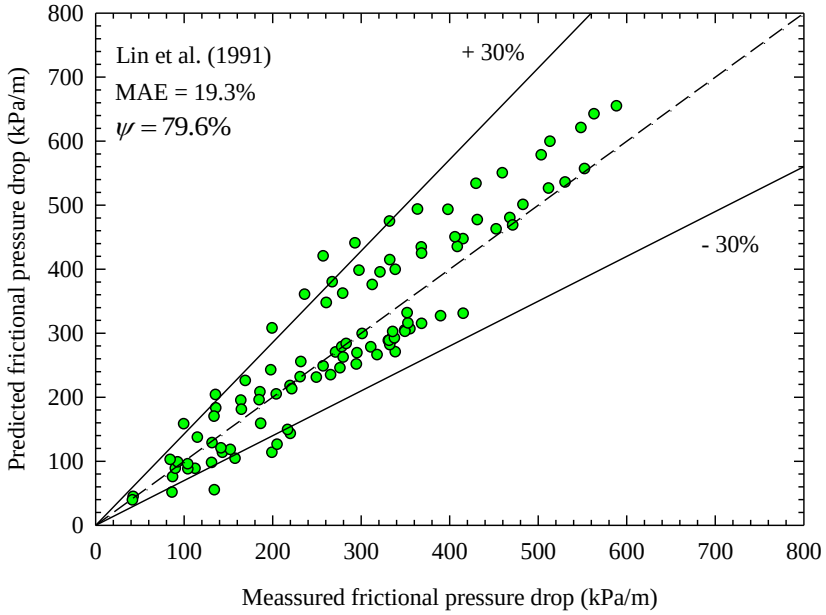

Figure 5.28 The comparison of the experimental data with existing correlation proposed by Lin et al. (1991)

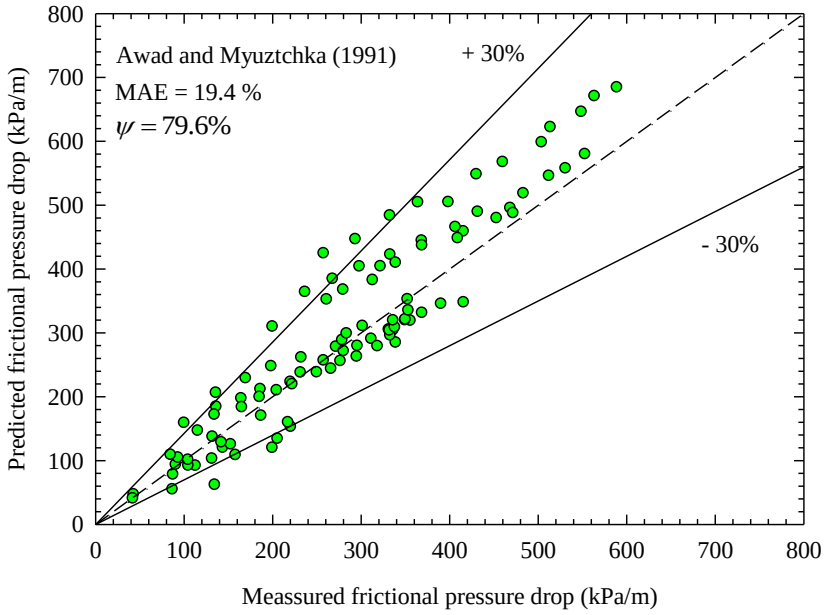

Figure 5.29 The comparison of the experimental data with existing correlation proposed by Awad and Myuztchka (2008)

For separated flow model which was found to be less predictable with the experimental data, the frictional pressure gradient of vapor-liquid two-phase flow is corrected by relationship between the two-phase frictional multiplier, ϕ_l^2, and Martinelli parameter X^2 which can be obtained from the frictional pressure gradients two-phase, liquid and vapor flow components as follows:

$$\left(\frac{\Delta P}{\Delta z}\right)_F = \phi_l^2 \left(\frac{\Delta P}{\Delta z}\right)_l \tag{5.10}$$

where $(\Delta P/\Delta z)_l$ is a single-phase liquid pressure gradient and $(\Delta P/\Delta z)_F$ represent two-phase frictional pressure gradient.

The Martinelli parameter, X^2, is given by

$$X^2 = \frac{\left(\Delta P / \Delta z\right)_l}{\left(\Delta P / \Delta z\right)_v} \tag{5.11}$$

where $\left(\Delta P/\Delta z\right)_l$ is a single-phase vapor pressure gradient.

For the two-phasemultiplier, Lockhart and Martinelli (1949) suggested that ϕ_l^2 is a function of Martinelli parameter:

$$\phi_l^2 = 1 + \frac{C}{X} + \frac{1}{X^2} \tag{5.12}$$

The constant C in the above equation is the parameter that represents the interactional effect of two-phase flow condition. Previously proposed correlations for frictional pressure drop in a microchannel have been developed by modifying the $C-\text{value}$ in the separated flow model were compiled and summarized in the table 5.3. Moreover, the assessment of all correlations based on the separated flow model used for comparison in this study, is shown in the Table 5.4.

Table 5.4 Two-phase frictional pressure gradient correlation based on the separated flow model

Author(s)	Equations
Lockhart-Martinelli (1949)	$C = 5$, for laminar-liquid, laminar-vapor $C = 12$, for laminar-liquid, turbulent-vapor $C = 10$, for turbulent -liquid, laminar-vapor $C = 20$, for turbulent -liquid, turbulent -vapor
Mishima and Hibiki (1996)	For rectangular channel, $C = 21\left(1 - \exp\left(-319 D_{\mathrm{h}}\right)\right)$ For circular tube, $C = 21\left(1 - \exp\left(-333 D_{\mathrm{h}}\right)\right)$
Hwang and Kim (2006)	$C = 0.227\,\mathrm{Re}_{\mathrm{lo}}^{0.452}\, X^{-0.32} Co^{-0.82}$ Where $Co = \dfrac{\left(\sigma/\left(\rho_{\mathrm{l}} - \rho_{\mathrm{v}}\right) g\right)^{1/2}}{D_{\mathrm{h}}}$
Qu and Muddawar (2003)	$C = 21\left(1 - \exp\left(-319 D_{\mathrm{h}}\right)\right)\left(0.00418 G + 0.0613\right)$
Lee and Garimella (2008)	$C = 2566 G^{0.5466} D_{\mathrm{h}}^{0.8819}\left(1 - \exp\left(-319 D_{\mathrm{h}}\right)\right)$
Zhang et al. (2010)	$C = 21\left(1 - \exp\left(-0.142/Co\right)\right)$

Table 5.5 Assessment of the separated model with different correlations

Correlation's	MAE (%)	Percentage of data within ±30% range
Lockhart-Martinelli (1949)	72.8	4.9
Friedel (1979)	32.5	52.4
Mishima and Hibiki (1996)	39.4	21.4
Hwang and Kim (2006)	24.1	75.3
Qu and Muddawar (2003)	55.9	41.7
Lee and Garimella (2008)	29.2	71.8
Zhang et al. (2010)	31.5	37.9

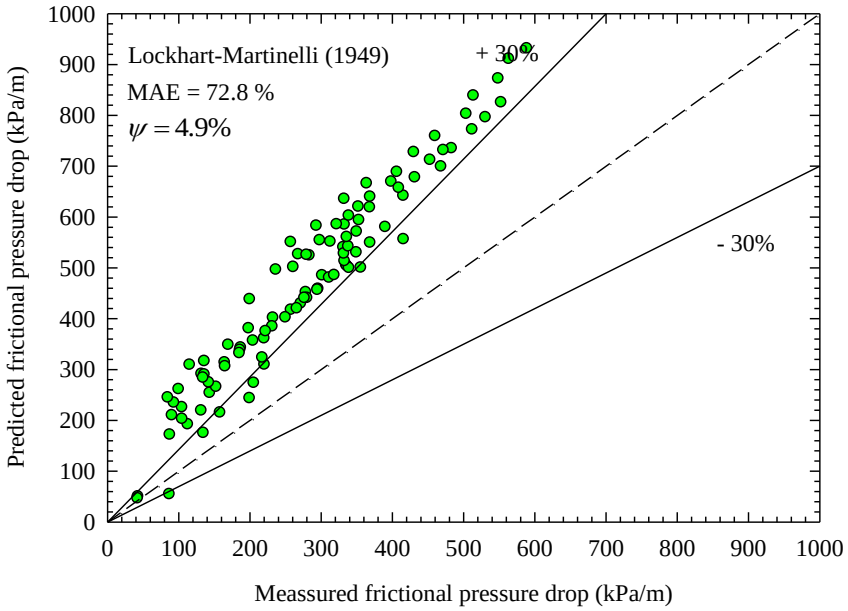

Figure 5.30 The comparison of the experimental data with existing correlation proposed by Lockhart-Martinelli (1949)

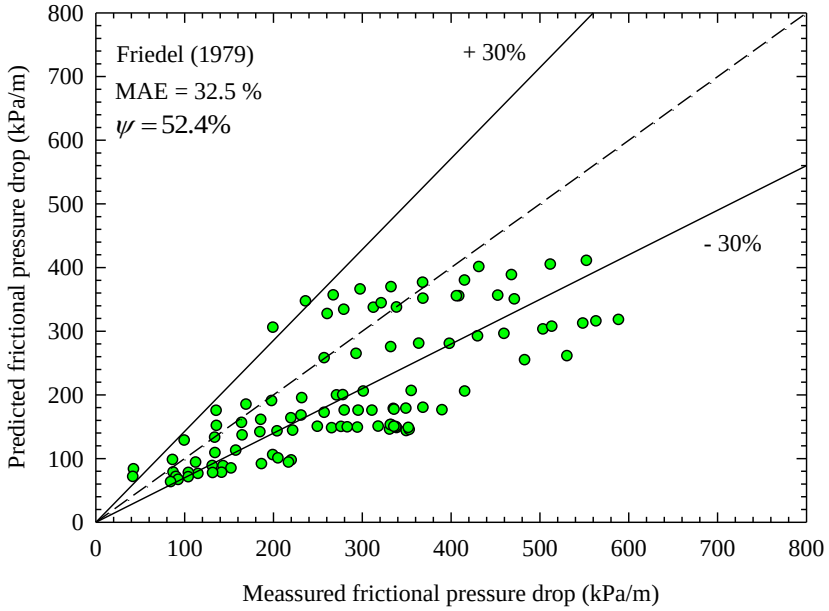

Figure 5.31 The comparison of the experimental data with existing correlation proposed by Friedel (1979)

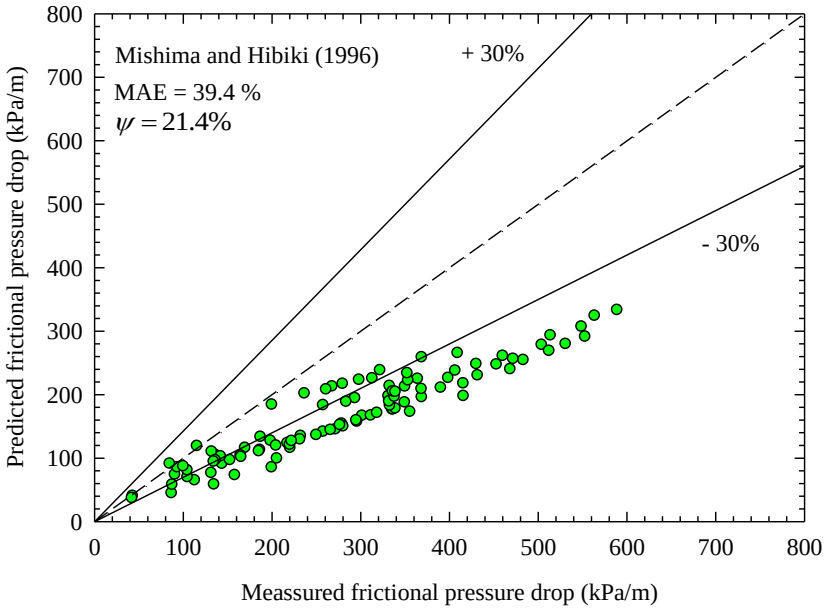

Figure 5.32 The comparison of the experimental data with existing correlation proposed by Mishima and Hibiki (1996)

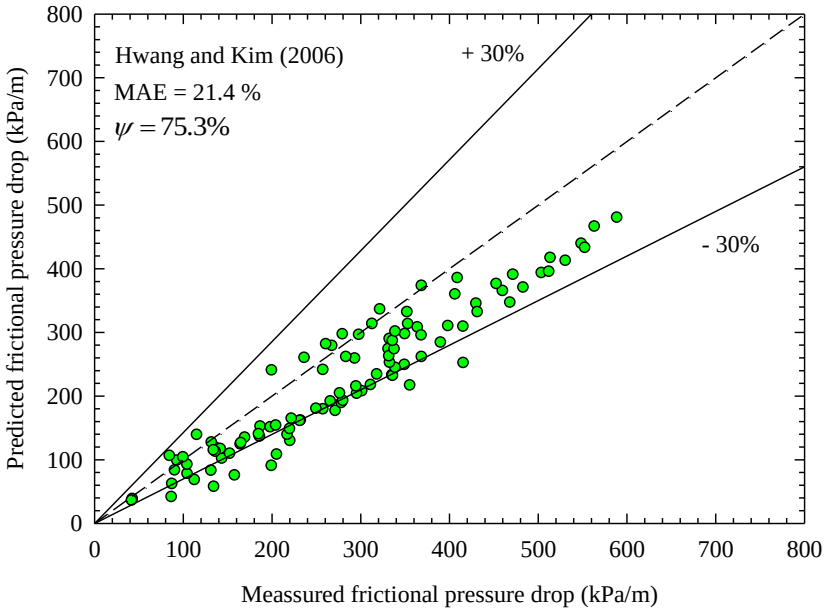

Figure 5.33 The comparison of the experimental data with existing correlation proposed by Hwang and Kim (2006)

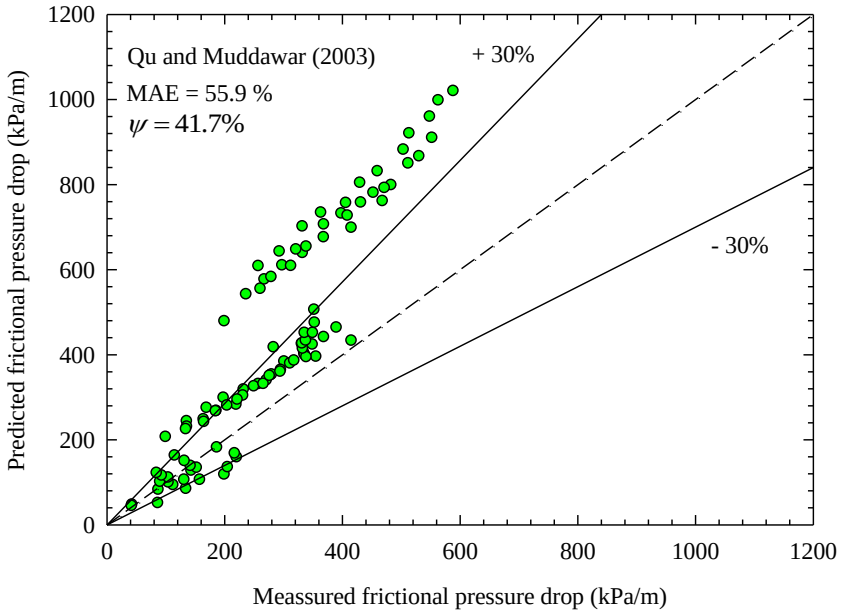

Figure 5.34 The comparison of the experimental data with existing correlation proposed by Qu and Muddawar (2003)

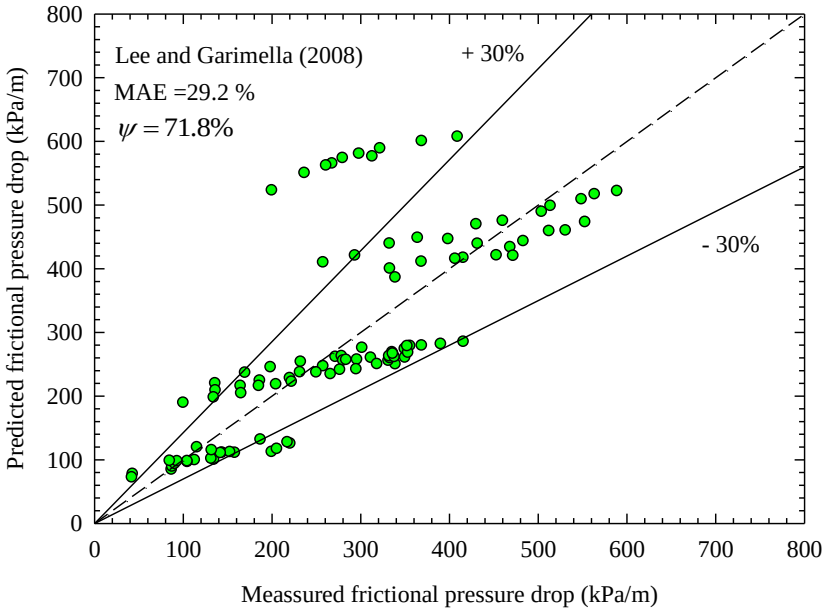

Figure 5.35 The comparison of the experimental data with existing correlation proposed by Lee and Garimella (2008)

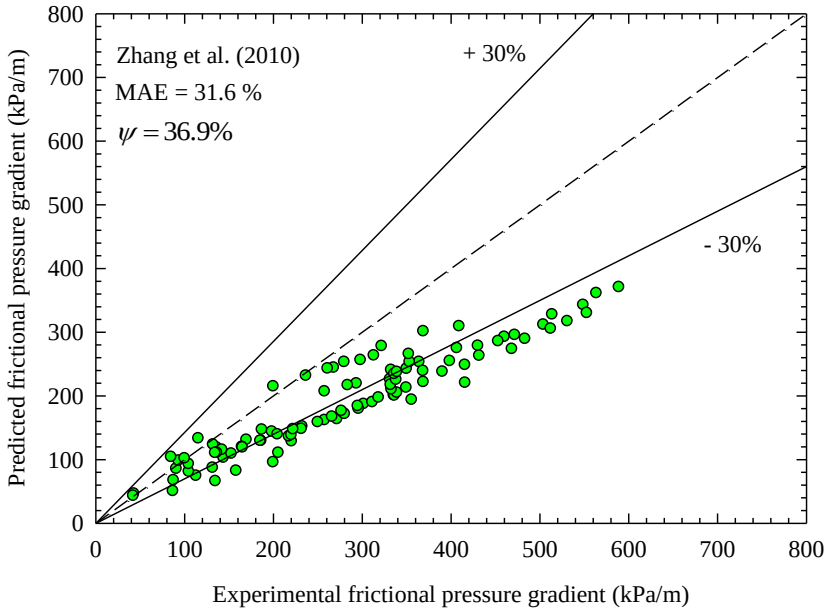

Figure 5.36 The comparison of the experimental data with existing correlation proposed by Zhang et al. (2010)

5.3.5 Proposed frictional pressure drop correlation

The Lockhart and Martinelli (1949) and Hwang and Kim (2006) methods are modified to develop a new pressure drop correlation for the present test section. The value of the constant, *C*, proposed by Chisholm (1973) varying from 5 to 20, depends on the flow conditions of the vapor and liquid. The relationships of the two-phase multiplier with the two-phase multiplier with the Martinelli parameter are plotted in Fig. 5.37. As shown in this figure, most of the measured data are in the region between C=5 and C=12. Hwang and Kim (2006) proposed the correlation for predicting the parameter C as follows:

$$C = 0.227\,\mathrm{Re}_{lo}^{0.452}\,Co^{-0.82}\,X^{-0.32} \tag{5.13}$$

Where Re_{lo} represents the all-liquid Reynolds number, Co is the confinement number, and X is a Martinelli parameter.

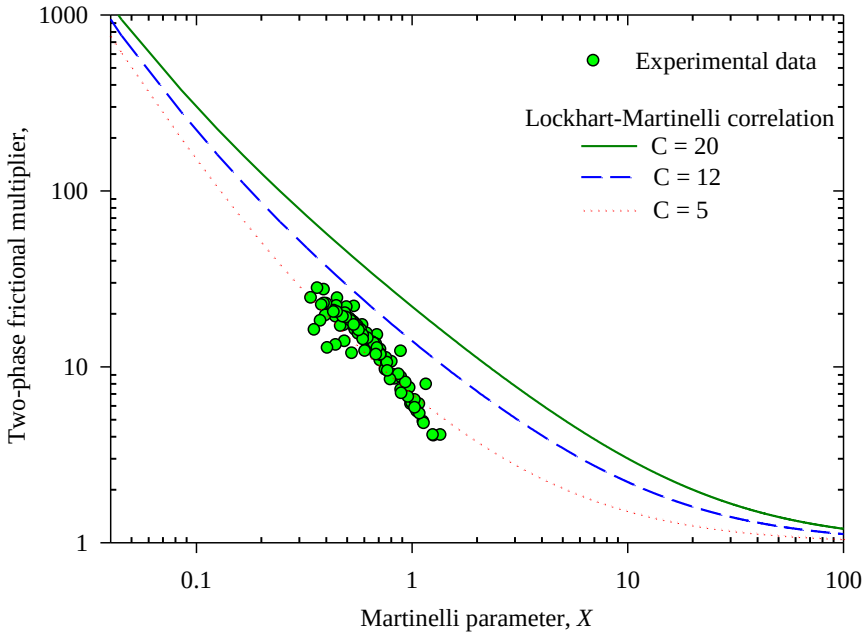

Figure 5.37 Martinelli parameter versus the two-phase frictional multiplier

A correlation in the form proposed by Hwang and Kim (2006) is developed from experimental data for predicting the two-phase multiplier, as shown in Eq. (5.14):

$$C = 0.4129\,\mathrm{Re}_{lo}^{0.02}\,Co^{3.19}\,X^{-0.48} \tag{5.14}$$

Comparison of the experimental frictional pressure gradient with the predicted frictional pressure gradient is shown in Fig. 5.38. This figure shows that the majority of the data falls within ±15% of the proposed correlation.

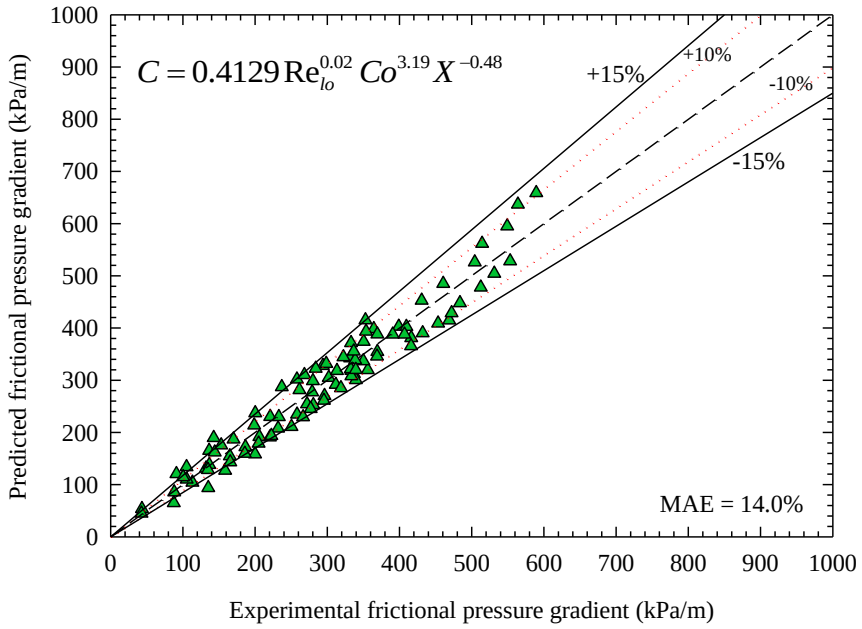

Figure 5.38 Predicted frictional pressure gradient using the proposed correlation versus the experimental data